quenched and the NiS beads were extracted and dissolved in 12 N HCl. The HCl solution was filtered through a cellulose membrane that traps insoluble Os sulfide. The cellulose membranes were then dissolved and standard Os distillation techniques or, later in the study, solvent extraction [A. S. Cohen and F. G. Water, *Anal. Chem.* **332**, 269 (1996)] were used to purify the Os, followed by microdistillation to further purify the Os. Blanks are 1 pg per gram of sample fused and have $^{186}Os/^{188}Os = 0.1199 \pm 0.0002$, and $^{187}Os/^{188}Os = 0.125 \pm 0.005$. Corrections to the sample ratios using these values are well within the uncertainties quoted in Table 1. Total procedural yields were 75 to 95 weight %. For Re and Os concentration determinations, 1- to 2-g samples of powder were spiked and dissolved in aqua regia in Carius tubes [S. B. Shirey and R. J. Walker, *Anal. Chem.* **67**, 2136 (1995)] to obtain sample spike equilibration followed by distillation or solvent extraction. Negative thermal ionization mass spectrometer procedures for unspiked high precision Os and spiked Re and Os measurements are presented elsewhere [(*7*) and references therein]. For high-precision Os analyses, we used a multicollector dynamic Faraday cup mode. Beam voltages ranged from 50 to 150 mV on ^{186}Os and ^{187}Os for at least 100 ratios to achieve the desired internal precision of 40 to 80 parts per million (2σ) on $^{186}Os/^{188}Os$. Tungsten trioxide, a possible interference at masses 232 and 234 ($^{184}Os/^{188}Os$ and $^{186}Os/^{188}Os$, respectively), was monitored via mass 232 (232/236 ratio) and was not observed under the run conditions. Multiple analyses of a Johnson and Matthey standard solution measured in this way gave external precisions of $^{186}Os/^{188}Os = 0.1198473 \pm 40$ and $^{187}Os/^{188}Os = 0.1137830 \pm 50$ ($n = 38$) during the course of the study.

20. N. H. Sleep, *J. Geophys. Res.* **95**, 6715 (1990).
21. J. E. Snow and L. Reisberg, *Earth Planet. Sci. Lett.* **133**, 411 (1995); T. Meisel, R. J. Walker, J. W. Morgan, *Nature* **383**, 517 (1996).
22. The $^{186}Os/^{188}Os$ of the proposed outer core component could not be much greater than the calculated value of 0.119852, assuming $\leq$1 weight % core addition to a plume. Crystallizing the inner core with proportionally greater or lesser partition coefficients for Re, Pt, and Os could lead to greater or lesser enrichment in ^{186}Os and ^{187}Os. However, enrichments would necessarily also be reflected in lower Os concentrations in the outer core (*7*). Although the outer core could be more radiogenic, if the lower mantle has approximately the same Os concentration as the upper mantle, the effects would be diluted by the mantle component.
23. S. B. Shirey and R. J. Walker, *Annu. Rev. Earth Planet. Sci.* **26**, 423 (1998).
24. The upper mantle average would be Pt at 6.54 ng/g based on an Os abundance of 3.3 ng/g (*11*) and a chondritic Pt/Os ratio of 1.984 [data on enstatite chondrites from (*9*)].
25. M.-J. Hertogen, M.-J. Janssens, H. Palme, *Geochim. Cosmochim. Acta* **44**, 2125 (1980); S.-J. Barnes, A. J. Naldrett, M. P. Gorton, *Chem. Geol.* **53**, 303 (1985); B. J. Fryer and J. D. Greenough, *Can. J. Earth Sci.* **29**, 2329 (1992); G. E. Brugmann *et al.*, *Geochim. Cosmochim. Acta* **57**, 2001 (1993).
26. G. Ravizza and D. Pyle, *Chem. Geol.* **141**, 251, 1997.
27. M. D. Norman and M. O. Garcia, unpublished data.
28. The 1.8-Ga altered ocean basalt is estimated to have a $\gamma_{Os} \cong 4000$ and sediment is estimated to have a $\gamma_{Os} \cong 400$ (*16*). See Figure 2 for end-member parameters for mixing calculations.
29. A. D. Brandon, R. A. Creaser, R. W. Carlson, S. B. Shirey, *Science* **272**, 861 (1996); M. Rehkämper, A. N. Halliday, D. Barfod, J. G. Fitton, J. B. Dawson, *Science* **278**, 1595 (1997); M. Humayun, *Trans. Am. Geophys. Union* **78**, F737 (1997).
30. G. Schmidt, H. Palme, K.-L. Kratz., *Geochim. Cosmochim. Acta* **61**, 2977 (1997).
31. M. F. Roden, T. Trull, S. R. Hart, F. A. Frey, *ibid.* **58**, 1431 (1994).
32. A. Tsuru, thesis, University of Maryland, College Park (1997).
33. Supported by National Science Foundation grants EAR-CSEDI 968703 and EAR-CSEDI 970986. Os-Ir alloys were kindly provided by A. M Clarke of the British Museum. T. Mock is gratefully thanked for his help with the mass spectrometry. Many conversations with M. Humayun and J. Lassiter helped clarify arguments presented in this paper. We thank W. McDonough and two anonymous journal reviewers.

18 February 1998; accepted 22 April 1998

Distribution of Rock, Metals, and Ices in Callisto

J. D. Anderson,* G. Schubert, R. A. Jacobson, E. L. Lau, W. B. Moore, W. L. Sjogren

Radio Doppler data from a single encounter (C3) of the Galileo spacecraft with Callisto, the outermost Galilean moon of Jupiter, indicated that Callisto was probably undifferentiated. Now, similar data from a second encounter (C9) corroborate this conclusion, but more accurate data from a third encounter (C10) indicate that the rock and ice within Callisto have partially, but not completely, separated. Callisto may be differentiated into a rock-metal core less than 25 percent of Callisto's radius, an outer layer of clean ice less than 350 km thick, and a middle layer of mixed rock and ice. Models in which ice and rock are mixed all the way to the center of Callisto are also consistent with the data.

During the primary Galileo Orbiter mission, three close flybys (C3, C9, C10) of Callisto provided data on this moon's gravitational field (*1*). Using radio Doppler data generated by the Deep Space Network (DSN) at three 70-meter stations located at Goldstone, California (DSS14), near Madrid, Spain (DSS63), and near Canberra, Australia (DSS43), and using nonlinear weighted least squares (*2*), we determined the second-degree coefficients in the standard spherical harmonic expansion of the gravitational potential, V (*3*).

In principle, the rotational and tidal distortions of Jupiter's Galilean satellites are separately excited and separately measurable. Thus it is possible to infer the degree of differentiation of each satellite in two independent ways (*4*). For a satellite such as Callisto, in synchronous rotation with its orbital period, equilibrium theory predicts that the gravitational coefficient $J_2 \equiv -C_{20}$ is exactly 10/3 of C_{22} [see (*3*) for the definition of C_{20} and C_{22}]. Any significant deviation from this relationship indicates that the assumption of hydrostatic equilibrium is not appropriate. However, because the three flybys did not provide a global coverage of the satellite's gravitational field (Table 1), an independent determination of J_2 and C_{22} was impossible. We applied the 10/3 constraint for all fits to the data.

The flyby geometry was more favorable for C3 than for C9 or C10, because along-track and cross-track components of the Doppler shift could be detected. For C9, the spacecraft passed directly behind Callisto (an Earth occultation), and could not communicate with stations on Earth during the occultation. As a result, there is a gap of about 11 min in the C9 data at closest approach. The altitude of the spacecraft above Callisto at occultation ingress was 1473 km and at egress was 1103 km. For C10 the spacecraft passed directly in front of Callisto, and radio Doppler data were obtained before, during, and after closest approach (Fig. 1). However, any gravitational perturbations for C9 and C10 were detected by the Callisto-centered trajectory bending only, while for C3 the bending and the velocity perturbation along the orbital path were detected.

The sensitivity of the radio Doppler data to Callisto's gravity depends on whether or not the data were coherent with atomic frequency standards at the DSN stations. This coherency was achieved only when the spacecraft radio system was locked to a signal from a DSN station by means of its S-band transponder. Otherwise, the data were referenced to the spacecraft's crystal oscillator with its inherently poor frequency stability, unknown frequency bias, and unknown frequency drift, in comparison to atomic frequency standards. In fitting the C3 and C9 noncoherent data we included the bias and drift as parameters in the model. However, because the bias and drift were negligible for the atomic-referenced coherent data, they were not included in the C10 model. Even though the geometry was more favorable for C3, the coherent data made C10 a better candidate for a reliable determination of Callisto's gravitational field.

The least-squares solution for J_2 and C_{22} from the C3, C9, and C10 data, analyzed independently (Table 1), depends on the assumption that all other harmonics in the

J. D. Anderson, R. A. Jacobson, E. L. Lau, W. L. Sjogren, Jet Propulsion Laboratory, California Institute of Technology, Pasadena, California 91109–8099, USA.
G. Schubert and W. B. Moore, Department of Earth and Space Sciences, Institute of Geophysics and Planetary Physics, University of California Los Angeles, California 90095–1567, USA.

*To whom correspondence should be addressed.

potential function V are zero. The coefficient μ represents the correlation between J_2 and C_{22} from the post-fit covariance matrix. Another fit to all the Doppler data from the three encounters, along with ground-based astrometric data on the positions of all four Galilean satellites and optical navigational data from Voyager and Galileo missions to Jupiter, yielded the following results in units of 10^{-6}: $J_2 = 31.1 \pm 4.5$; $C_{21} = 0.0 \pm 0.4$; $S_{21} = 0.0 \pm 0.8$; $C_{22} = 10.5 \pm 0.4$; $S_{22} = -0.7 \pm 0.3$; $\mu = 0.202$.

Unlike the three independent fits (Table 1), all five second-degree gravitational coefficients were included in the combined fit, although all other harmonics were excluded. The a priori constraint that J_2 is exactly 10/3 of C_{22} is retained within its 1-σ error bound. There is a low positive correlation $\mu = 0.202$ between J_2 and C_{22} after the fit, but this does not imply they are independently determined. A large variation in J_2 outside its error limits, even setting it equal to zero and leaving it out of the fit, produces an insignificant change to C_{22} and has essentially no effect on the Doppler residuals after the fit.

We used $C_{22} = 10.5 \pm 0.4$ from the combined fit (*5*), and an average density of 1830 kg m^{-3}, to infer the internal structure of Callisto on the assumption that the moon's spherical harmonic degree-2 gravitational field is due to the equilibrium tidal and rotational ellipsoidal distortion of a satellite in synchronous rotation with its orbital period. Under these conditions, C_{22} is related to the rotational parameter q_r by

$$C_{22} = (3\alpha q_r)/4 \qquad (1)$$

where q_r is a measure of the forcing for rotational flattening of the satellite ($q_r = 36.69 \times 10^{-6}$ for Callisto) and α is a dimensionless response coefficient that depends on the distribution of density with depth inside the satellite ($\alpha = 0.5$ for constant density) (*4*). For $C_{22} = 10.5 \pm 0.4$ in units of 10^{-6}, α is 0.382 ± 0.015. From equilibrium theory and the value of α, it follows that Callisto's axial moment of inertia C, normalized to MR^2, is $C/MR^2 = 0.359 \pm 0.005$. This value of C/MR^2 is less than 0.4, the value of C/MR^2 for a sphere of constant density, and requires some concentration of mass toward the center of Callisto. The value of C/MR^2 from the C3 flyby (Table 1) is consistent with an object of constant density, and we inferred from the C3 data alone that Callisto was not differentiated (*6*). The present data, however, require some differentiation of the satellite.

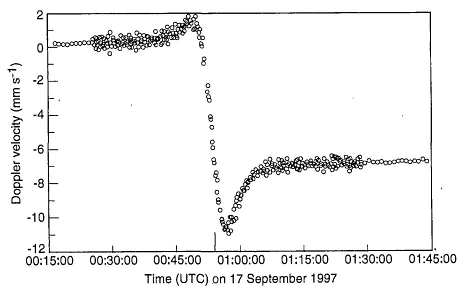

Fig. 1. Doppler residuals (observed Doppler velocity minus model Doppler velocity) from C10 for a model in which Callisto's gravitational field is represented only by GM and J_2. All other gravitational harmonics are zero. The large residuals indicate that the model is incomplete. Although not shown, by adding one gravitational harmonic, C_{22}, the residuals are distributed randomly about zero Doppler velocity and their magnitude is reduced by about a factor of 43. Hence by including GM, J_2, and C_{22} in the model, the Doppler data can be fit to within the noise level (0.3 mm s^{-1}, one σ, at a sample interval of 10 s). The smaller residuals near the beginning and end of the plot are due to a larger sample interval of 60 s, and hence a longer Doppler integration time, compared to the sample interval of 10 s for the data surrounding the spacecraft's closest approach to Callisto (indicated by the single large tick mark).

Table 1. Callisto Encounter Geometry and Gravity Results. The location of the spacecraft's closest approach is given in the first three rows, where longitude is measured west of the Callisto-Jupiter direction and altitude is referenced to a sphere of radius R = 2403 km (*3*). The SEP angle is the elongation between the sun and Jupiter. For SEP angles greater than 90°, the minimum amount of phase noise is introduced into the S-band (2.3 GHz) radio wave as it propagates through solar plasma (*21*). The next three rows give the direction cosines of the Doppler line of sight for the Callisto flyby trajectory at closest approach. The cross-track component is aligned with the Callisto-spacecraft direction, the along-track component is aligned with the spacecraft's Callisto-centered velocity vector, and the normal component is aligned with the spacecraft's Callisto-centered orbital angular momentum vector. The last four rows give the results of the data analysis, with each flyby analyzed independently. The estimated errors, both in the table and in the text, are taken directly from the covariance matrix associated with the data analysis. They are based on an assumed standard error of 2 mm s^{-1} for noncoherent Doppler and 1 mm s^{-1} for coherent Doppler at a sample interval of 60 s. For data sampled at 10 s the error is increased by the square root of six. A weighting algorithm is applied that down weights the data for lower elevation angles at the DSN stations. The assumed errors for the data are about 8 times larger than the standard error of the data noise (Fig. 1). Consequently, all estimates of error should be taken as realistic, reflecting possible contributions from systematic error and from a reddening of the noise spectrum by solar plasma.

	C3	C9	C10
Latitude (deg)	13.2	−2.3	4.6
Longitude (deg)	77.9	259.2	78.7
Altitude (km)	1136	418	535
SEP (deg)	61.1	132.3	138.8
	Direction cosines for line of sight		
Cross Track	−0.655	0.994	−0.996
Along Track	0.734	−0.104	0.051
Normal	0.178	−0.037	0.078
Coherent Doppler?	No	No	Yes
J_2 (10^{-6})	47.7 ± 11.5	49.3 ± 13.0	33.9 ± 4.7
C_{22} (10^{-6})	14.3 ± 3.2	14.8 ± 3.7	10.4 ± 0.3
μ	0.9128	0.9327	0.1372
C/MR^2	0.407 ± 0.039	0.412 ± 0.044	0.358 ± 0.004

The ice in a model of Callisto with a constant ice-rock fraction would undergo transformation with depth to higher density phases (*7*), such that the density of an undifferentiated model of Callisto would actually increase with depth and the C/MR^2 of the model would be 0.38 (*8*). This is more than 4 σ away from the nominal value of $C/MR^2 = 0.359$ reported here, indicating that Callisto must be partially differentiated.

Consistent with the few constraints we have on Callisto's internal structure (mean density and moment of inertia), we explore simple two- and three-layer models of its interior density. We use a forward modeling approach, solving Clairaut's equation for the distortion of a satellite with a given internal structure. Even the simple parameterizations adopted here are underconstrained, so we present families of possible hydrostatic internal structures consistent with the observed mean density and C_{22}.

The two-layer models have two free parameters which we have chosen to be the density of each layer (Fig. 2). The interior density ranges from the mean density of Callisto to the mean density of Io, 3560 kg m^{-3}, while the outer shell density ranges from the density of ice up to the mean density of Callisto. Models which have the observed value of C_{22} fall between two end members: a relatively pure ice outer shell about 300 km thick overlying a mixed ice and rock interior of density near 2300 kg m^{-3}, and a thick (about 1000 km) mixed ice and rock outer shell with a density near 1600 kg m^{-3} overlying a rock-metal core with a density near that of Io.

The two-layer models are a subset ($R_{core}/R_{Callisto}$ = 0) of the three-layer models shown in Fig. 3. We have chosen to use the mean density of Io for the density of the core in the three-layer models, reducing the number of free parameters to three: outer and middle layer density and core radius. The family of solutions satisfying the observations is shown as a surface in this three-dimensional parameter space. Models with an outer layer of clean ice (density less than 1100 kg m^{-3}) are constrained to have an outer layer less than about 350 km thick overlying a deep (more than 1000 km thick) middle layer of mixed rock and ice (with a density between 1700 and 2300 kg m^{-3}) which in turn surrounds a core that may be up to 50% of Callisto's radius. Larger cores require thinner outer shells and more ice-rich (lower density) middle layers. If both the outer and middle layers are ice-rock mixtures of different densities, the range of models is greater, with the nearly vertical lines on the surface in Fig. 3 showing the range of variation for a given core size. Models in which the base of the outer layer is defined by the stability of ice I closely follow the blue-green boundary in Fig. 3 (models with smaller cores have more extended stability ranges for ice I which transforms to either ice II or ice III at a pressure near 200 MPa) (9).

We have also explored more completely differentiated three-layer models with a metallic Fe-FeS core (density 5150 kg m^{-3}). Such models require ice-rich middle layers, with densities less than 2500 kg m^{-3}. An intimate mixture of rock and ice is inconsistent with the formation of a metallic core by separation of rock and metal, since metal separation requires temperatures far in excess of the melting point of ice. Thus we conclude that, unlike Ganymede (10), Callisto does not have a metallic core.

The heat associated with the separation of ice and rock in models with a core will melt a significant fraction of the ice: a core 25% Callisto's radius melts 10% of the ice upon differentiation, while a core 40% Callisto's radius would melt nearly 50% of the ice. Because complete ice-rock separation is unavoidable if too much of the ice melts (11) a large core (more than about 25% of Callisto's radius) is unlikely, given the observed C_{22}.

The models we have explored lead us to conclude that the ice and rock-metal that make up Callisto have never completely separated. The observations do not require an ice-free core, but are consistent with a core of up to 25% Callisto's radius as discussed above. Surrounding this core are an ice-rock middle layer with a density near 2000 kg m^{-3} and an outer shell which is less than about 350 km deep if it is relatively clean ice but may be deeper if it is also an ice-rock mixture.

If a satellite as ice-rich as Callisto is capable of maintaining elastic stresses over geologic time (for instance, to support a fossil tidal bulge) then the assumption of a hydrostatic figure is incorrect, and the moment of inertia could be smaller than inferred from C_{22} using the equilibrium assumption. As discussed above, the gravity passes were unable to independently determine the ratio of J_2 to C_{22} to demonstrate hydrostatic equilibrium, and there is no topographic control on the actual shape. The amount of ice-rock separation we report is therefore a lower limit, and Callisto could be hiding further differentiation beneath a strong elastic shell.

Incomplete separation of ice and rock is consistent with other observations of the satellite. Callisto does not have an intrinsic magnetic field (12), which is consistent with the absence of a metallic core. Callisto's surface shows no sign of endogenic activity, which is consistent with an undifferentiated or partially differentiated interior (7). Recent high-resolution Galileo images of Callisto reveal no volcanic or tectonic features that could be associated with internal activity (13). In contrast, Ganymede, whose gravitational and magnetic fields suggest complete differentiation of the satellite into a metallic core, rocky mantle, and icy crust (14), has a surface that has been heavily modified by endogenic tectonism (7, 15). High-resolution Galileo coverage of Callisto is incomplete, and some areas identified in Voyager data as possibly modified by volcanic or internal tectonic activity (16), may yet turn out to be areas of degraded ancient tectonism associated with the early partial differentiation of Callisto (13). It is unlikely, however, that Callisto could have undergone substantial internal differentiation while leaving little or no evidence of this on its surface. Callisto is dynamically isolated from the three inner Galilean satellites, which are locked in a three-way orbital resonance discovered by Laplace (17). Callisto, the farthest Galilean satellite from Jupiter, therefore lacks the tidal heat source that has driven the volcanic activity (7, 18) and differentiation (19) of Io, the closest Galilean satellite to Jupiter, and that may

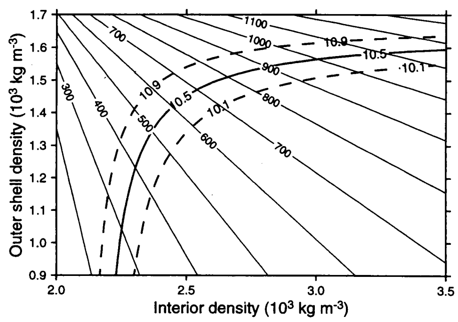

Fig. 2. Two-layer models of Callisto's interior structure. The density of the inner layer is given on the *x*-axis and the density of the outer layer is given on the *y*-axis. Models which satisfy the nominal C_{22} value of 10.5 (in units of 10^{-6}) plot along the thick solid line, and models within the 1-σ error on C_{22} plot between the dashed lines. The thin solid lines give the thickness of the outer layer in 100-km increments.

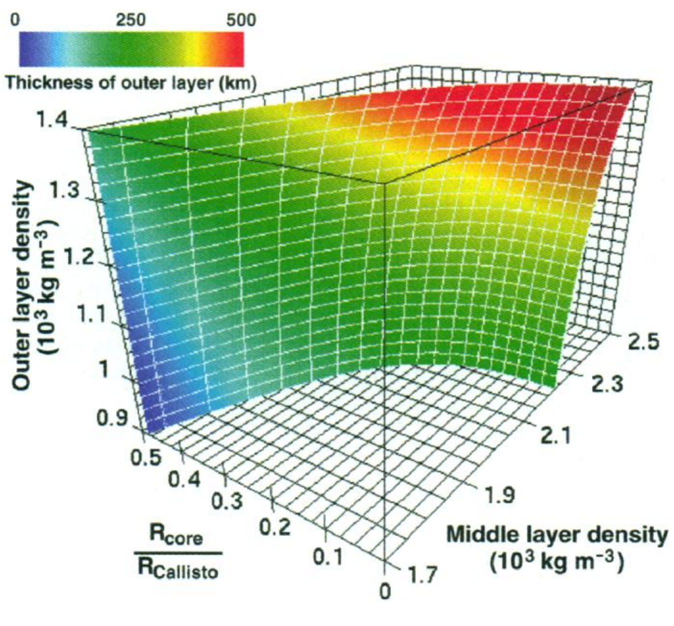

Fig. 3. Three-layer models of Callisto's interior structure. The axes of the figure are core radius (as a fraction of Callisto's radius), outer layer density, and middle layer density. The core has a density of 3500 kg m^{-3}, corresponding to the mean density of Io. Models satisfying the nominal C_{22} value of 10.5 (in units of 10^{-6}) plot on the colored surface in three-dimensional parameter space, with the color giving the thickness of the outer layer as shown by the color bar. Models with zero core radius plot at the right-hand edge of the surface and are equivalent to the two-layer models shown in Fig. 2.

have played a role in the differentiation of Europa and Ganymede (*7, 14, 20*). The possibility that tidal heating due to Jupiter could have influenced the evolution of Ganymede, which is closer to Jupiter than Callisto, but not of the similarly large and massive Callisto is one way to reconcile the differentiation of Ganymede with the partial differentiation of Callisto (*6*).

REFERENCES AND NOTES

1. The first encounter (C3) occurred on 4 November 1996 at 11:47:09, the second (C9) occurred on 25 June 1997 at 13:47:50, and the third (C10) occurred on 17 September 1997 at 00:18:55, where the encounter times are expressed in Universal Time Coordinated (UTC) at the spacecraft, and the encounter designation Cn refers to an encounter with Callisto on the spacecraft's *n*th orbital revolution of Jupiter.
2. See, for example, T. D. Moyer, *Tech. Rep. No. TR 32-1527* (Jet Propulsion Laboratory, Pasadena, CA, 1971); B. D. Tapley, in *Recent Advances in Dynamical Astronomy*, B. D. Tapley and V. Szebehely, Eds. (Reidel, Dordrecht, Netherlands and Boston, MA, 1973), pp. 396–425; J. D. Anderson, in *Experimental Gravitation*, B. Bertotti, Ed. (Academic Press, New York, 1974), pp. 163–199.
3. W. M. Kaula, *Theory of Satellite Geodesy* (Blaisdell, Waltham, MA, 1966). The expression for V is

$$V(r,\phi,\lambda) = \frac{GM}{r}\left[1 + \sum_{n=2}^{\infty}\sum_{m=0}^{n}\left(\frac{R}{r}\right)^{n} \times (C_{nm}\cos m\lambda + S_{nm}\sin m\lambda)P_{nm}(\sin\phi)\right]$$

where M is the satellite's mass and G is the gravitational constant, $G = 6.6728 \pm 0.0016 \times 10^{-11}$ m^3 kg^{-1} s^{-2} [see E. R. Cohen and B. N. Taylor, *Phys. Today* **49**, BG9 (1996)]. The spherical coordinates (r, ϕ, λ) are referred to the center of mass, with r the radial distance, ϕ the latitude and λ the longitude on the equator. Callisto's reference radius R is 2403 km [see M. E. Davies *et al.*, *Celes. Mech.* **53**, 377 (1992)]. P_{nm} is the associated Legendre polynomial of degree n and order m, and C_{nm} and S_{nm} are the corresponding coefficients determined from the data.
4. W. B. Hubbard and J. D. Anderson, *Icarus* **33**, 336 (1978); S. F. Dermott, *ibid.* **37**, 310 (1979); V. N. Zharkov, V. V. Leontjev, A. V. Kozenko, *ibid.* **61**, 92 (1985); S. Mueller and W. B. McKinnon, *ibid.* **76**, 437 (1988); G. Schubert, D. Limonadi, J. D. Anderson, J. K. Campbell, G. Giampieri, *ibid.* **111**, 433 (1994).
5. Our adopted solution for Callisto's gravitational field fits the C9 and C10 Doppler data to within the noise level, but there is a residual signal at about the 3 mm s^{-1} level in the fit to the C3 data. This signal, of unknown origin, explains the difference between the C_{22} values from the independent fits for C3 and C10 (Table 1). Because the C9 data can be fit with the adopted gravitational field, the differences between the C9 and C10 independent fits are reconciled. We attribute the larger value of C_{22} from the independent C3 fit to systematic error in the noncoherent data, but we are not able to rule out completely the possibility that C3 is right and our adopted solution is wrong.
6. J. D. Anderson, E. L. Lau, W. L. Sjogren, G. Schubert, W. B. Moore, *Nature* **387**, 264 (1997).
7. Undifferentiated models of Callisto involve transformations of ice to phases such as ice II, ice VI, and ice VIII at depth in the satellite [M. J. Lupo, *Icarus* **52**, 40 (1982); J. Leliwa-Kopystynski, L. Makkonen, O. Erikoinen, K. J. Kossacki, *Planet. Space Sci.* **42**, 545 (1994)]. Other phases of ice (ice III and ice V) may occur depending on the radial profiles of temperature and pressure in the model interiors. The depths of the ice phase changes also depend on the temperature and pressure profiles [G. Schubert, D. J. Stevenson, K. Ellsworth, *Icarus* **47**, 46 (1981); G. Schubert, T. Spohn, R. T. Reynolds, in *Satellites*, J. A. Burns and M. S. Matthews, Eds. (Univ. of Arizona Press, Tucson, AZ, 1986), pp. 629–688].
8. W. B. McKinnon, *Icarus* **130**, 540 (1997).
9. P. V. Hobbs, *Ice Physics* (Clarendon Press, Oxford, 1974).
10. J. D. Anderson, E. L. Lau, W. L. Sjogren, G. Schubert, W. B. Moore, *Nature* **384**, 541 (1996).
11. A. J. Friedson and D. J. Stevenson, *Icarus* **56**, 1 (1983).
12. K. K. Khurana, M. G. Kivelson, C. T. Russell, R. J. Walker, D. J. Southwood, *Nature* **387**, 262 (1997).
13. J. Klemaszewski, personal communication.
14. G. Schubert, K. Zhang, M. G. Kivelson, J. D. Anderson, *Nature* **384**, 544 (1996).
15. S. W. Squyres and S. K. Croft, in *Satellites*, J. A. Burns and M. S. Matthews, Eds. (Univ. of Arizona Press, Tucson, AZ, 1986) pp. 293–341; W. B. McKinnon and E. M. Parmentier, in *Satellites*, J. A. Burns and M. S. Matthews, Eds. (Univ. of Arizona Press, Tucson, AZ, 1986) pp. 718–763; R. T. Pappalardo *et al.*, in preparation; G. C. Collins, J. W. Head, R. T. Pappalardo, *Geophys. Res. Lett.* **25**, 233 (1998); L. M. Prockter *et al.*, in preparation.
16. P. M. Schenk, *J. Geophys. Res.* **100**, 19023 (1995).
17. J. H. Lieske, *Astron. Astrophys.* **82**, 340 (1980).
18. S. J. Peale, P. Cassen, R. T. Reynolds, *Science* **203**, 892 (1979); M. Segatz, T. Spohn, M. N. Ross, G. Schubert, *Icarus* **75**, 187 (1988); M. N. Ross and G. Schubert, *ibid.* **64**, 391 (1985).
19. L. Keszthelyi and A. McEwen, *Icarus*, in press; A. S. McEwen *et al.*, in preparation.
20. R. Malhotra, *Icarus* **94**, 399 (1991); A. P. Showman and R. Malhotra, *ibid.* **127**, 93 (1997); A. P. Showman, D. J. Stevenson, R. Malhotra, *ibid.* **129**, 367 (1997).
21. R. Woo and J. W. Armstrong, *J. Geophys. Res.* **84**, 7288 (1979).

22. We thank the referee, W. B. McKinnon, for a careful review of the manuscript and for several suggestions that improved the interpretive discussion. This work was sponsored by the Galileo Project and was performed at the Jet Propulsion Laboratory, California Institute of Technology, under contract with NASA. G.S. and W.B.M. acknowledge support by grants from NASA through the Galileo Project at JPL and the Planetary Geology and Geophysics program.

24 February 1998; accepted 14 May 1998

Detection of Atomic Deuterium in the Upper Atmosphere of Mars

Vladimir A. Krasnopolsky,* Michael J. Mumma, G. Randall Gladstone

High-resolution spectroscopy of Mars' atmosphere with the Hubble Space Telescope revealed the deuterium Lyman α line at an intensity of 23 $\pm$ 6 rayleighs. This measured intensity corresponds to $HD/H_2 = 1.5 \pm 0.6 \times 10^{-4}$, which is smaller by a factor of 11 than HDO/H_2O. This indicates that fractionation of HD/H_2 relative to that of HDO/H_2O is not kinetically controlled by the rates of formation and destruction of H_2 and HD but is thermodynamically controlled by the isotope exchange $HD + H_2O \leftrightarrow HDO + H_2$. Molecular hydrogen is strongly depleted in deuterium relative to water on Mars because of the very long lifetime of H_2 (1200 years). The derived isotope fractionation corresponds to an estimate of a planetwide reservoir of water ice about 5 meters thick that is exchangeable with the atmosphere.

Dissociation of water vapor with subsequent escape of H, H_2, and O is the primary mechanism of water loss from Mars. It is believed that Earth, Venus, and Mars were formed by the same rocky and icy planetesimals (*1*), which resembled meteorites and comets in their composition, respectively. These planets are thus expected to have initially had the same chemical and isotope composition. If the mass of the terrestrial ocean (having a global-equivalent depth of 2.7 km) is scaled by the planetary mass ratio, the expected initial water abundance on Mars is a layer about 1 km thick, assuming that this layer covers the entire martian surface. Geological estimates (*2, 3*) favor 300 to 500 m of water ice. The current estimated rate of water loss of 1.2 m per billion years (*4–6*) would not significantly affect this reservoir. However, the rate of escape of H, H_2, and O could have been much higher on early Mars (*7*), and a feature that should reflect the integrated loss of martian water is the D/H ratio. The measured D/H ratio in Mars' water vapor exceeds that of terrestrial water by a factor of 5.5 and corresponds to $HDO/H_2O = 1.7 \times 10^{-3}$ (*8, 9*). It is generally believed that enrichments in heavy isotopes are mostly due to the preferential escape of light isotopes. The enrichment is especially strong for D because D is twice as massive as H.

D/H ratios measured in martian meteorites vary from 1.9 to 5.4 times Earth's ratio (*10*). These meteorites are thought to have been ejected from Mars by impact. High D/H ratios in martian crustal water (represented by D/H measured in martian mete-

V. A. Krasnopolsky, Department of Physics, Catholic University of America, Washington, DC 20064, USA, and NASA Goddard Space Flight Center (GSFC), Greenbelt, MD 20771, USA.
M. J. Mumma, NASA GSFC, Greenbelt, MD 20771, USA.
G. R. Gladstone, Southwest Research Institute, San Antonio, TX 78228, USA.

*To whom correspondence should be addressed at NASA/GSFC, Code 690.2, Greenbelt, MD 20771, USA. E-mail VKras@lepvx3.gsfc.nasa.gov